

The X_{co} factor in PDRs

Bachelor Thesis

Michael van Schaik
S2223937

Supervisor: Gisela Esplugues
Co-supervisor: Stephanie Cazaux

Second reader: Marco Spaans

Rijksuniversiteit Groningen
Kapteyn Astronomisch Instituut
13 July 2016

Contents

Abstract

1. Introduction	3
2. Observational X_{co} determination	3
2.1.1. Virial method	3
2.1.2. Measuring the amount of CO	4
2.1.3. Extinction	5
2.1.4. Dust emission	6
2.1.5. Gamma rays	6
2.2. Observational results	6
3. Project Goal	7
3.1. PDRs	8
4. PDR code	9
5. Method	10
6. Results	12
6.1 CO abundance	12
6.2 Gas temperature	13
6.3 Cooling rate	14
6.4 H_2 column density	15
6.5 Integrated intensity	15
6.6 The X_{co} factor	16
6.7 Surface chemistry effect	17
7. Comparisons	18
7.1 Comparison with observations	18
7.2 Comparison with previous works	19
8. Conclusions	21
8.1 Future work	21
9. References	22

Abstract

The mass of molecular clouds can be measured through the amount of H_2 since this is the most abundant species in this kind of region, however, H_2 cannot be directly observed since it does not have a permanent dipole. Other techniques to measure the mass of molecular clouds are therefore required. Since CO represents the second most abundant species in molecular clouds and can be easily observed with radio-telescopes, it has traditionally been used to measure the mass of molecular clouds through the X_{co} factor. Although the X_{co} factor considers the amount of gas-phase CO, the role of dust grains and the chemistry taking place on the surface is key to determine the abundances of CO. The aim of this study is to analyze, from a theoretical point of view, the influence of surface chemistry and of other parameters, such as density and intensity of radiation field, on the X_{co} factor using the recently updated Meijerink PDR code. We also compare our results with observations and with previous works.

1. Introduction

The chemical composition of the interstellar gas is relevant in many branches of Astronomy and determines which telescopes can be used for its observation. The different atoms and molecules determine the thermal balance of the gas, which in turn influences several characteristics, such as the mass and multiplicity of the stars that will be formed. In order to understand how a cloud will evolve, it is important to estimate its mass. There are many processes going on at the same time (such as ionization, dissociation and recombination). Only recently models are starting to consider dust surface chemistry. Recent results (Esplugues et al. 2016) show that the chemical composition of the interstellar medium (ISM) is significantly altered when surface chemistry is taken into account.

In the particular case of Giant Molecular Clouds (GMCs), the mass is mostly in the form of H_2 , since this is the most abundant molecule. However, since H_2 does not have permanent dipole moment, it is very difficult to observe this molecule directly, because of the weakness of its lines. Alternative methods to measure the mass of GMCs are needed.

One method to determine the mass of H_2 gas is to use CO. The gas in a GMC is composed of various elements such as H and He. Heavier elements are also present in the cloud with C and O as the most abundant heavy elements. Together they form CO, which is an observable molecule with radio telescopes. The lowest CO transition has a low excitation temperature of 5.53 K, so it can be excited even in cold clouds. The transition $j = 1 \rightarrow 0$ at 2.6 mm is particularly interesting, since our atmosphere is reasonably transparent at that wavelength. That means that this transition can be observed from the Earth. The first observation of this molecule was made in 1970 (Wilson, Jefferts & Penzias 1970). These authors observed the Orion nebula using the 36 feet NRAO antenna at Kitt Peak, Arizona. CO and H_2 can be related through the conversion factor X_{co} .

2. Determining the X_{co} factor

2.1.1. Virial method

One method to determine the X_{co} is by using virial techniques. This method is based on the virial theorem. A fundamental question is to address whether the giant molecular clouds are virialized or not. If we suppose that the cloud is not virialized, we have two possibilities: the cloud has too much kinetic energy or the cloud has too little kinetic energy. In the first case the cloud will dissipate, while in the second case it will collapse and form new stars. Those new stars will add new energy to the cloud and make it more virialized. If we take these scenarios into account, we can reason that most clouds will be in or close to virial equilibrium.

The mass of molecular clouds can be determined from their size and velocity dispersion (Solomon et al. 1987). From the mass of the cloud, its luminosity (L_{co}) can be determined through the relation CO

mass-luminosity. The relation between the mass and L_{CO} shows a very strong power-law fit, see Figure 1. This fit matches very well the theoretical relation between the virialized mass and L_{CO} .

With this method, important assumptions need to be considered. One of the biggest issues is to determine the exact size of the cloud. In practice, this depends on the value taken for the minimum emission that is used to determine the edge. Another related issue is that two or more clouds may be entangled with each other and need to be separated correctly. The separation will become especially difficult for extra-galactic observations due to the resolution available. As a final issue, the virial method assumes that CO is uniformly distributed all over the cloud. In reality, there are parts in the cloud where there is more CO compared to other parts, and its excitation can be different depending on the conditions of the cloud. In certain parts of the cloud, gas can also become optically thick which represents a problem if the gas deeper into the cloud does not have the same composition.

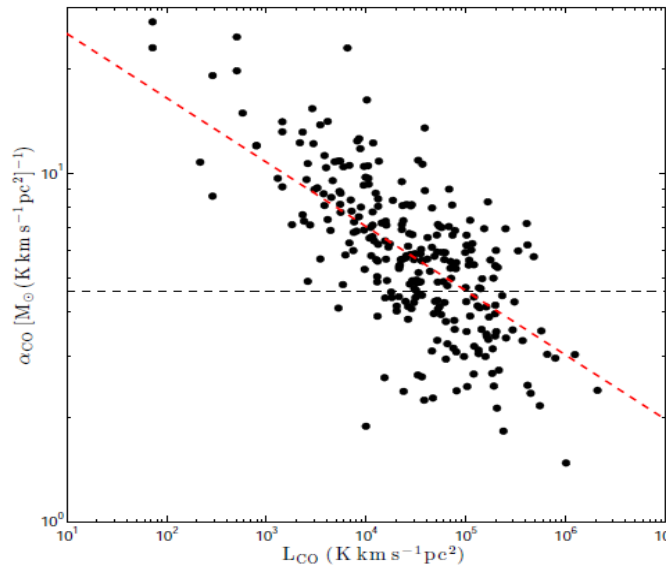


Figure 1: Relation between mass and CO luminosity of GMCs in the Milky way. The red dashed line indicates the relation mass and luminosity. The black dashed line is the nominal value at $L_{CO} = 10^5 \text{ K km s}^{-1} \text{ pc}^2$ (Bolatto & Wolfire 2013)

2.1.2. Measuring the amount of CO

Another way to determine the H_2 column density (mass per unit area integrated along a path) is to use optically thin tracers, such as isotopologues (molecules consisting of an atom with at least one neutron difference compared to the standard molecule). The emission should be optically thin at far-infrared wavelengths to use it determine a column density.

^{13}CO is a good and very often used isotopologue. The ratio between ^{13}C and ^{12}C is known to be about 69 in the solar neighborhood and about 50 at 4 kpc from the galactic center (Wilson 1999). ^{13}CO becomes optically thick around a visual extinction of 5 magnitudes (mag). The column densities of ^{13}CO can be used to determine those for CO. To do this, both the temperature and the density of the cloud along the line of sight are needed. Local Thermal Equilibrium (LTE) is often assumed, which means that there is a single excitation temperature that describes the population distribution among the possible levels along the line of sight. Another assumption is that ^{13}CO and ^{12}CO have the same T_{ex} when excitations are mainly due to collisions between particles. This assumption is not valid when radiative trapping plays an important role in the excitation of the CO because ^{13}CO and ^{12}CO do not have similar optical depth. Using the isotope ratio between ^{13}C and ^{12}C and the ^{13}CO column density, the column density of ^{12}CO can be calculated.

2.1.3. Extinction

Extinction can also be used to directly determine the X_{CO} , assuming that the observing bands have spatially uniform extinction properties and that the relation between extinction and column density is valid (Bolatto & Wolfire 2013). This gives a relation between the CO column density and the extinction. The result is a linear relation up to an extinction of 10 mag with the best fit up to an extinction of 4 mag. At higher extinctions, CO freezes on dust mantles and is thus no longer in the gas phase. The relation between the CO column density and extinction improves when CO freezing on mantles is taken into account (Pineda et al. 2010). Extinction mapping can only be used on nearby galactic clouds because a clear line of sight is needed and it should be possible to see individual stars behind them.

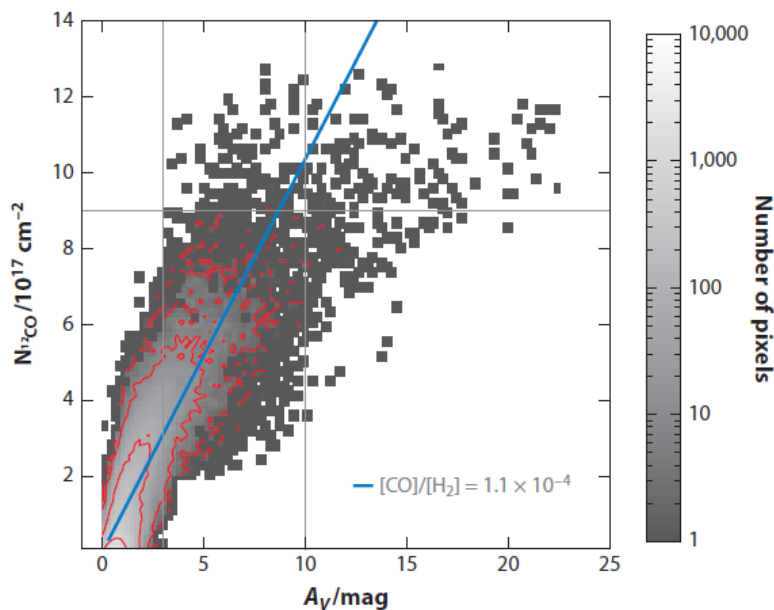


Figure 2: Relation between the CO column density and the extinction in the Taurus molecular cloud. The blue line shows the “average” linear relation (Pineda et al. 2010).

2.1.4. Dust emission

Dust emits in the far infrared wavelength range and can be used to trace the gas distribution. With the dust spectral energy distribution, it is possible to determine, assuming that there is a constant dust emissivity per gas nucleon, the optical depth, which should be proportional to the total gas column density. There is a strong relation between the optical depth and the number density of H (Boulanger et al. 1996). The optical depth depends on the gas to dust ratio and the optical properties of dust. The dust emissivity per nucleon can be determined from the lines of sight dominated by the atomic gas.

2.1.5. Gamma rays

Cosmic rays can interact with interstellar matter resulting in pion production. Gamma rays from pion production can penetrate deep into the molecular cloud. In these clouds, gamma rays decay through collisions between particles. This creates diffuse gamma ray emission that can be used to count the nucleons. When the differences in emissivity between the molecular cloud and atomic gas are taken into account, the same methods described for extinction (section 2.3) can be used to determine X_{co} factor.

To carry out observations of gamma rays can be difficult due to the high angular resolution needed. The distribution of the gamma ray emission does not follow the distribution of gas, but it is larger at places where the gamma rays are penetrating the cloud (Murphy et al. 2012). Due to this, the determination of the cloud characteristics becomes harder as they highly depend on the location where cosmic rays penetrate the cloud.

2.2. Observational results for X_{co}

The different methods described above lead to the X_{co} values shown in Table 1. All the methods agree within a factor 5 with each other. One thing that is noted by multiple studies is that the X_{co} factor is up to ten times lower in the galactic center (Bolatto & Wolfire 2013). These measurements were done using gamma rays, dust emission, virial mass, and all converge to the same value. This lower value in the galactic center is likely due to hotter clouds and differences in velocity dispersion (Bolatto & Wolfire 2013). There are also some differences in high-latitude clouds. While different parts of the Milky Way have been observed, there are not many observations of the outer part of the galaxy. The observations that were made had high X_{co} values. In the case of low abundances of CO, this molecule becomes a poor tracer of H₂. This is the case when the visual extinction (A_v) is lower than 2 mag. One explanation for this is that most of the carbon in the gas is not in the form of CO.

Method	$X_{\text{CO}}/10^{20}\text{cm}^{-2}$ (K km s^{-1}) ⁻¹	References
Virial	2.1	Solomon et al. (1987)
	2.8	Scoville et al. (1987)
Isotopologues	1.8	Goldsmith et al. (2008)
Extinction	1.8	Frerking, Langer & Wilson (1982)
	2.9–4.2	Lombardi, Alves & Lada (2006)
	0.9–3.0	Pineda, Caselli & Goodman (2008)
	2.1	Pineda et al. (2010b)
	1.7–2.3	Paradis et al. (2012)
Dust emission	1.8	Dame, Hartmann & Thaddeus (2001)
	2.5	Planck Collaboration XIX et al. (2011)
γ -rays	1.9	Strong & Mattox (1996)
	1.7	Grenier, Casandjian & Terrier (2005)
	0.9–1.9 ^a	Abdo et al. (2010c)
	1.9–2.1 ^a	Ackermann et al. (2011, 2012c)
	0.7–1.0 ^a	Ackermann et al. (2012a,b)

Table 1: Observational values for X_{co} in the Milky Way (Bolatto & Wolfire 2013 and references therein).

3. Project goal

The total H_2 mass can be estimated with the CO to H_2 conversion factor, X_{co} . In this work, the X_{co} factor for photo-dissociation regions (PDRs) will be determined. This factor is calculated using an PDR code that for the first time takes into account complete surface chemistry, which directly affects the chemical composition of the cloud (see section 4 for the full explanation of the code). We will study the effects of varying the density and the radiation field. The effects of surface chemistry are also examined by running the model with and without surface chemistry. This model results for X_{co} are then compared to the observational values and previous works that do not take surface chemistry into account. Improving the calculation of the X_{co} gives a better understanding of molecular cloud masses under different conditions.

3.1 PDRs

To carry out this project, an updated version of the Meijerink PDR code (Esplugues et al. 2016) has been used. This code was originally developed by (Meijerink & Spaans 2005). The code reproduces the typical conditions of PDRs. PDRs consist of ionized atoms, neutral gas and dust. Most of the mass of the gas and dust found in the Galaxy are in PDRs, which contain most of the mass in the ISM (Hollenbach & Tielens 1997). The most important heating source is far ultraviolet radiation (FUV) radiation from nearby massive stars. This radiation has a strong influence on the chemistry of the gas. The absorbed FUV radiation is re-emitted in the IR, making PDRs one of the major contributors to the IR radiation from the ISM. The other major contributors are: HII regions and dust excited by late-type stars that emit radiation in the IR (Hollenbach & Tielens 1997). The outer parts of the PDR get ionized by the radiation. As the extinction increases when we penetrate deep into the cloud, chemistry presents significant variations due to the attenuation of the FUV radiation. This produce a decrease of the temperature of the region. As a consequence, the ionization grade of species is lower as the visual extinction increases, and more complex molecule can be formed deep in the cloud (see Figure 3).

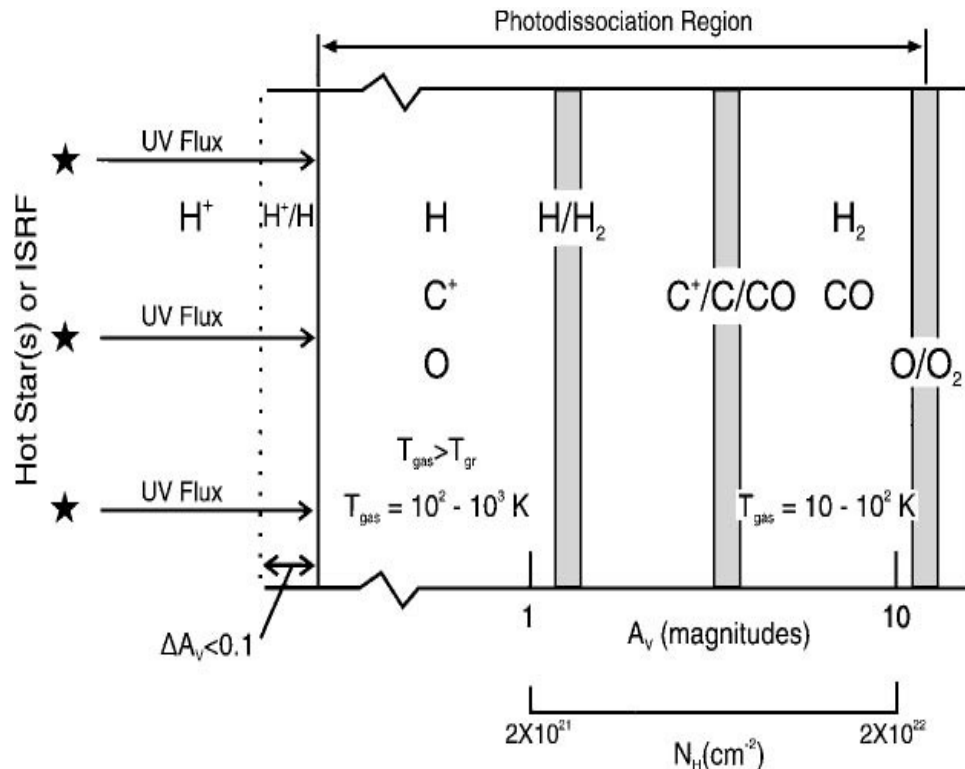


Figure 3: A schematic diagram of a photodissociation region. The PDR is illuminated from the left and it extends from the predominantly atomic surface region to the point where O_2 is not appreciably photo-dissociated ('10 visual magnitudes). Hence, the PDR includes gas whose hydrogen is mainly H_2 and whose carbon is mostly CO . Large columns of warm O , C , C , C^+ , and CO and vibrationally excited H_2 are produced in the PDR. The gas temperature T_{gas} generally exceeds the dust temperature T_{gr} in the surface layer (Hollenbach & Tielens 1997).

When studying chemistry of the interstellar medium, it is key to consider the role of dust grains as well. Dust grains are powerful catalysts for the formation of many species on their surfaces. The surface of the dust particles can be bare or can be covered by ice mantles. Strong radiation prevents the forming of ice mantles, resulting in bare grains (Meijerink et al. 2012). Deeper into the cloud most of the dust is covered by ice layer(s), which can be evaporated, enriching the gas-phase of the region. Important types of surface reactions are: adsorption (species are depleted onto dust grains), thermal desorption (solid species are released into the gas-phase due to the dust temperature), chemical desorption (solid species are released into the gas-phase due to chemical reactions), photo processes (photo-desorption and photo-dissociation), and cosmic ray processes (frozen molecules that get desorbed by cosmic rays). A more detailed description of these processes can be found in Esplugues et al. (2016).

4. The PDR code

Here we are going to study the X_{co} factor in PDRs and its variation depending on the type of PDR. For this purpose, we use the most recent version of the Meijerink PDR code (Esplugues et al. 2016). In particular, we simulate different types of PDRs by varying the density (n) and the intensity of the radiation field (G_0).

With respect to the chemical balance, this code considers 7503 gas-phase chemical reactions taken from the Kinetic Database for Astro-chemistry (KIDA; Wakelam et al. 2015). The gas-phase reactions are: bi-molecular reactions, charge-exchange reactions, radiative association, associative detachment, dissociative recombination, neutralization reactions, ion-neutral reactions, ionization or dissociation by UV photons and ionization or dissociation by cosmic ray particles or by secondary H_2 excitation. There are several heating and cooling mechanisms considered in the PDR code. The heating mechanisms considered are: the photoelectric effect on dust grains, carbon ionization heating, H_2 photo dissociation, heating by UV radiation, H_2 collisional de-excitation heating, gas-grain collisional heating, gas-grain viscous heating and cosmic-ray heating. The cooling mechanisms considered are: fine structure line cooling, meta stable-line cooling, recombination cooling and molecular cooling by CO , H_2 and H_2O (see Meijerink & Spaans 2005 for more details).

The inclusion of surface chemistry is the most recent addition to the Meijerink PDR code and it has been done by including 117 chemical reactions. The surface reactions are described in section 3.1 and the gas-phase reaction are described in the paragraph above. See Esplugues et al. (2016) for a complete list of these surface reactions.

As output, the Meijerink PDR provides the physical distance of each shell, the gas temperature, the dust temperature and the abundances of each species at each visual extinction (A_v).

5. Method

The X_{co} factor is defined as:

$$X_{\text{CO}} = N(\text{H}_2) / \int T_A(\text{CO}) dv \quad [\text{cm}^{-2} (\text{K km s}^{-1})^{-1}], \quad (1)$$

where $N(\text{H}_2)$ is the column density of H_2 and the denominator is the antenna temperature of CO integrated over all frequencies (e.g. Bell et al. 2006):

$$\int T_A(\text{CO}) dv = \frac{c^3}{2k\nu^3} I \quad [(\text{K km s}^{-1})^{-1}]. \quad (2)$$

In expression (2): k is the Boltzmann constant, ν is the frequency of CO(1-0) and c the speed of light. This integrated intensity (I) is given by expression (3) (Bell, Roueff & Williams 2006). The factor $1/2\pi$ takes into account that photons escape the cloud at the edge and not over the full 4π steradians. A is the CO(1-0) line emissivity at each depth in the cloud:

$$I = \frac{1}{2\pi} \int A(z) dz \quad [\text{erg s}^{-1} \text{ cm}^{-2} \text{ sr}^{-1}]. \quad (3)$$

There are, however, some extra steps that need to be made to get the quantities that are not provided by the PDR code, $N(\text{H}_2)$ and $A(z)$. $N(\text{H}_2)$ is done by integrating H_2 over the distance:

$$N(\text{H}_2) = \int n_{\text{H}_2} dz \quad [\text{cm}^{-2}]. \quad (4)$$

Since the PDR code provides the total emission strength of the cloud, which cannot be used to directly obtain X_{co} , we have to calculate the CO ($j = 1 \rightarrow 0$) transition by using :

$$A(z) = \frac{g_1}{g_0} n_0 A_{10} dE_{10} \beta_{\text{esc}} \left(\frac{S-P}{S} \right) e^{\frac{-dE_{10}}{k_b T_{\text{gas}}}} \quad [\text{erg cm}^{-3} \text{ s}^{-1}] \quad (5)$$

(Tielens & Hollenbach 1984), where n_0 is the number of CO molecules in the $j=0$ state, g is the degeneracy of the level, A_{10} is the Einstein coefficient for spontaneous emission, dE_{10} is the energy difference between the two states and β is the escape probability of an emitted photon from a semi infinite slab, $(S-P)/S$ takes into account the pumping by dust emission and the cosmic microwave background (CMB), with S being the source function and P the background radiation, k_b is Boltzmann constant and T_{gas} the temperature of the gas. β can be obtained using (Tielens & Hollenbach 1984):

$$\beta_{\text{esc}} = \frac{1 - e^{-2.34\tau}}{4.68\tau} \quad \text{for } \tau < 7 \quad (6)$$

and

$$\beta_{esc} = \left(4\tau \left(\ln \left(\frac{\tau}{\sqrt{\pi}} \right) \right)^{0.5} - 1 \right) \text{ for } \tau \geq 7. \quad (7)$$

β considers the fact that not all emitted photons reach the surface of the cloud. Some are instead reabsorbed and thus do not contribute to the net cooling. The escape probability depends on the opacity τ (Tielens & Hollenbach 1984):

$$\tau = 1.1 \cdot 10^{-14} N(CO) \text{ [cm}^{-2}\text{]}. \quad (8)$$

The source function describes the ratio between the absorption coefficient and the emission coefficient, so it gives a description of the absorbed and emitted photons along the cloud (Tielens & Hollenbach 1984):

$$S = \left(2 \frac{h\nu^3}{c^2} \right) \frac{1}{\left(e^{dE_{ul}/k_b T_{gas}} - 1 \right)} \text{ [erg s}^{-1} \text{ cm}^{-2} \text{ sr}^{-1} \text{ Hz}^{-1}\text{]}. \quad (9)$$

There are two other ways to excite CO in the cloud besides the UV radiation: the dust particles in the cloud that emit radiation in the infrared (IR) and the CMB. To consider this background radiation (P) we use:

$$P = B(\nu, T = 2.7 \text{ K}) + \tau B(\nu, T_{dust}) \text{ [erg s}^{-1} \text{ cm}^{-2} \text{ sr}^{-1} \text{ Hz}^{-1}\text{]}, \quad (10)$$

where B is the Planck function (Tielens & Hollenbach 1984). The CMB has a peak at $T = 2.7 \text{ K}$ and the dust uses the dust temperature (T_{dust}).

The following constants have been used in this work:

Name	Abbreviation	Value	Units
Boltzmann constant	k_b	$1.38 \cdot 10^{-16}$	erg/K
Frequency	ν	$1.15 \cdot 10^{11}$	1/s
Speed of light	c	$3 \cdot 10^{10}$	cm/s
Level energy difference	dE_{10}	5.56	K
Einstein coefficient for stimulated emission	A_{10}	$7.2 \cdot 10^{-8}$	1/s
degeneracy	g_1 and g_0	3 and 1	unit-less
Planck constant	h	$4.135 \cdot 10^{-15}$	K

Table 2: *Used constants in this work.*

Since the PDR output is a discrete array, to calculate the column density of H_2 and CO , a cumulative trapezoid integral has been used. In particular, a right Riemann sum has been used, where a loop takes into account the two regimes of β (Eqs. 6 & 7).

6. Results

In this section, we show the results obtained for different type of PDRs. All have solar metallicity and take surface chemistry into account unless stated otherwise, see Esplugues et al. (2016) for the initial abundances used.

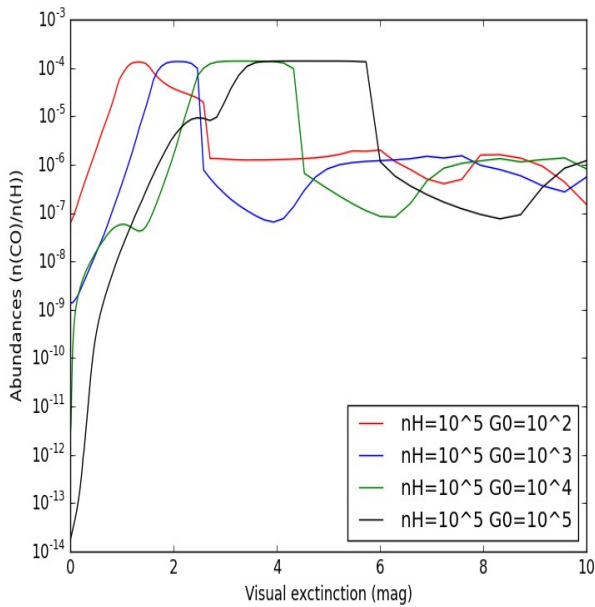


Figure 4: Relative abundances of CO for PDRs with constant density and different G_0 .

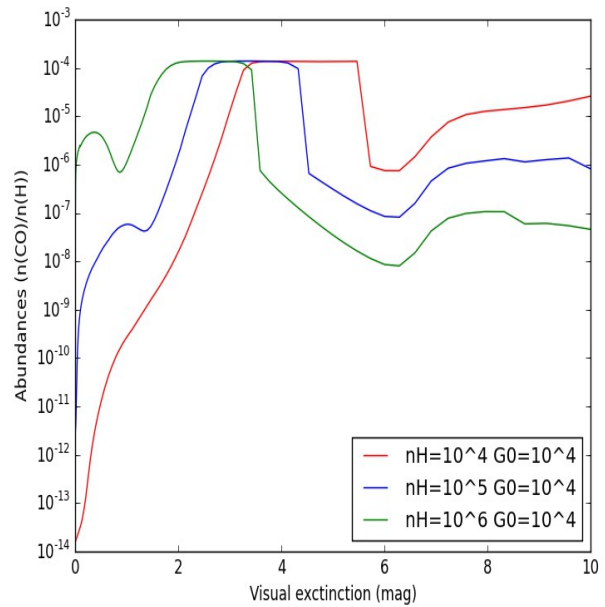


Figure 5: Relative abundances of CO for PDRs with constant G_0 and different density.

6.1. CO abundance

Figures 4 and 5 show the abundances of CO at various visual extinctions. In Figure 4, G_0 is varied and in Figure 5, the density is varied. We observe a peak in the CO abundance in all cases which appears at larger visual extinction (A_v) as the intensity of the radiation field increases or the density decreases. The difference in abundance between the peak and the rest of the curve is several orders of magnitude. It is

interesting to look at the fact that the peak is around 10^{-4} ($n_{\text{CO}}/n_{\text{H}}$) independent of density or radiation field. In these peaks most of the C is in the form of CO. The main influence of varying the density or the intensity of the radiation field of the PDR is, therefore, to determine the visual extinction at which the maximum abundance of CO is reached. Lower densities have CO abundance peaks deeper into the cloud and at the same time the distribution in the tails becomes larger, see Figure 5. In Figure 4 the peak becomes wider as the intensity of the radiation increases, because when n_{H}/G_0 decreases, radiation will penetrate deeper into the cloud, leading to more C in the atomic form.

6.2. Gas temperature

The temperature of the gas is shown in Figures 6 and 7 for different PDRs. There is a general trend for both figures where T decreases as A_v increases. An increase in radiation results in a higher overall temperature. At the difference in temperature decreases deeper into the cloud. The effect of density is not as pronounced; a lower density gives slightly higher temperatures since there is less material to heat up and the radiation can penetrate deeper into the cloud. There are sharp features in the graphs that can be produced by some artifact of the code.

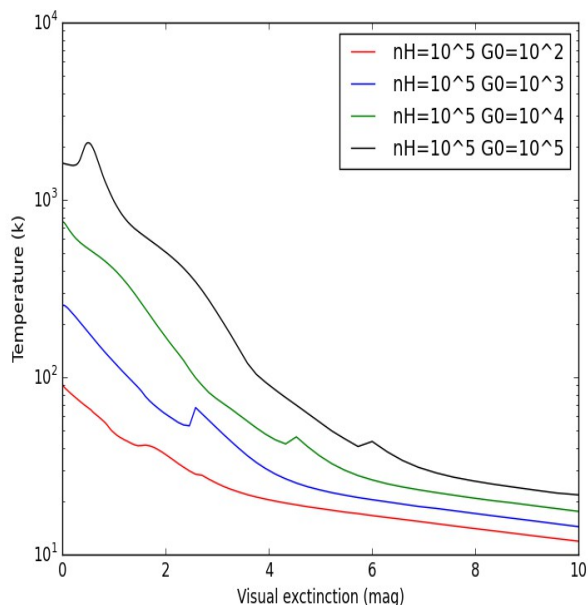


Figure 6: Gas temperature for different types of PDR with constant density and different G_0 .

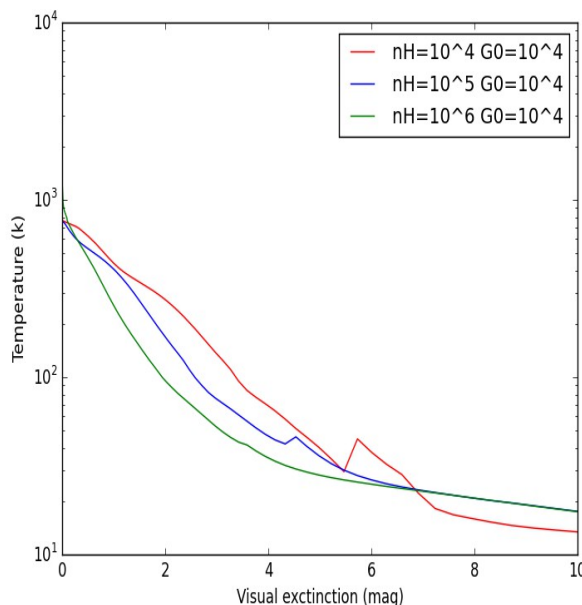


Figure 7: Gas temperature for different types of PDR with constant G_0 and different density.

6.3. Cooling rate

The CO cooling rates can be calculated using expression (5), leading to the results shown in Figures 8 and 9. In those figures, most of the cooling occurs at $A_v < 6$, which corresponds to the highest abundance of CO. In expression (5), show that the cooling linearly depend on the abundance of CO. The maximum cooling rates are between 10^{-23} and 10^{-26} [erg cm⁻³ s⁻¹]. After the peak is reached, the cooling slowly decreases. This is a consequence of the escape probability, since deeper into the cloud the opacity becomes higher and a lower amount of emitted photons reach the surface to contribute to the cooling. There is a significant drop in the cooling curves after the peak, this again is a result of the CO abundance at those points. The drop in CO abundance and the drop in the cooling rate occur at the same magnitude. At $A_v = 10$ mag, all the cooling rates agree with each other within a factor 2.

Increasing G_0 (see Figure 8) leads to a lower peak in the CO cooling rates, while at larger extinctions these rates sharply decreases. The peak value of the cooling rate only becomes slightly lower (factor 3) as G_0 increases. This is due to the escape probability being higher in the region of the peak. The effects of density are more pronounced. In particular, to increase the density leads to a cooling rate that can become 3 orders of magnitude higher, as shown in Figure 9. The region with peak emission shifts nearer to the surface of the cloud with higher densities, but the width of the curves where CO emission is important remains the same, around four magnitudes.

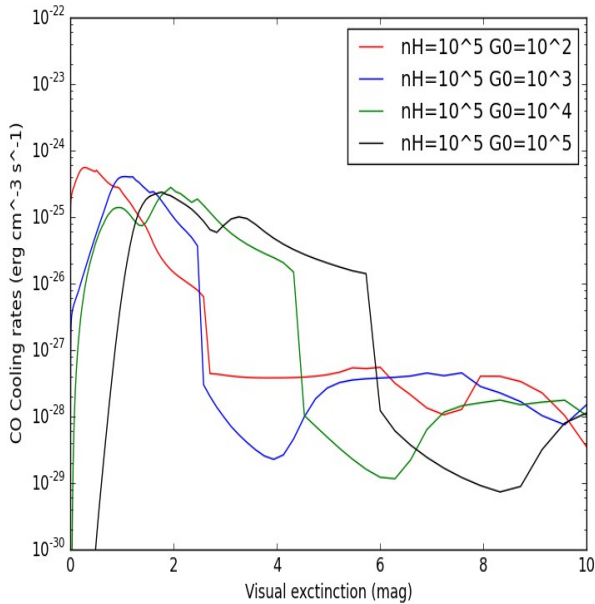


Figure 8: CO Cooling rates ($j = 1 \rightarrow 0$) for different types of PDR with constant density and varying G_0 .

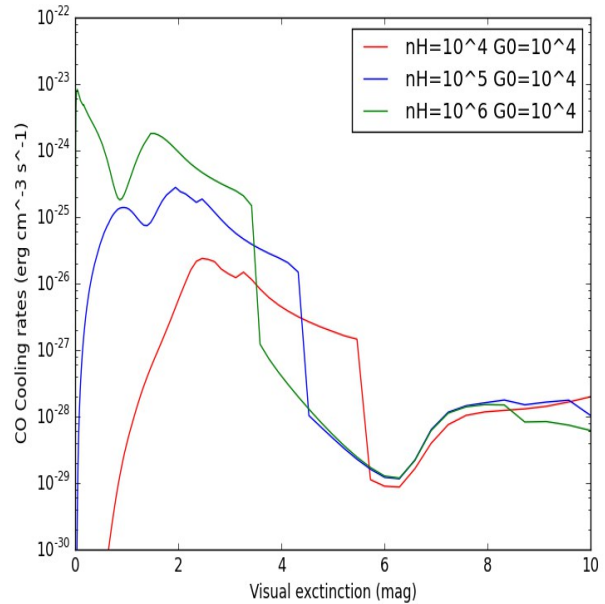


Figure 9: CO Cooling rates ($j = 1 \rightarrow 0$) for different types of PDR with constant G_0 and varying density.

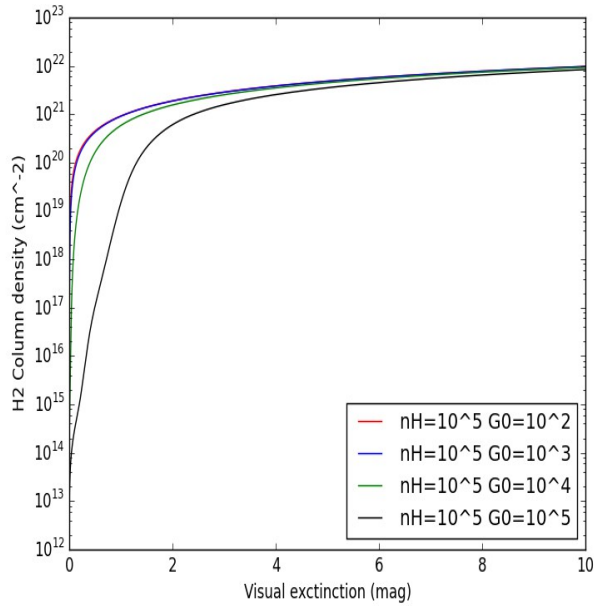


Figure 10: $N(H_2)$ for different types of PDR with constant density and varying G_0 .

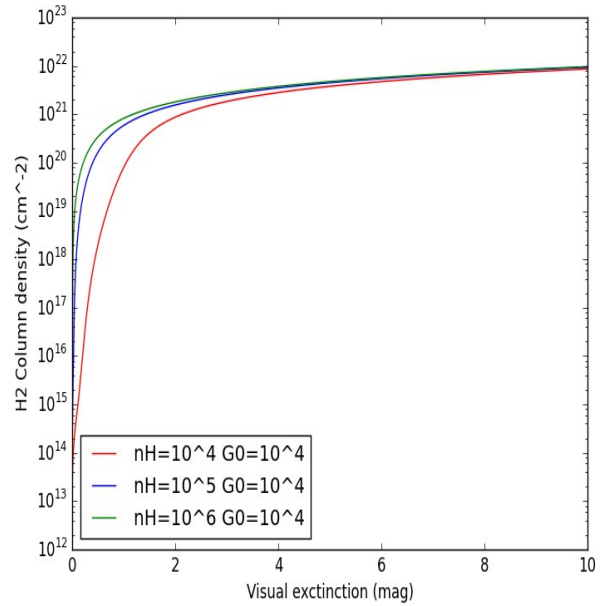


Figure 11: $N(H_2)$ for different types of PDR with constant G_0 and varying density.

6.4. H_2 column density

The H_2 column density is shown in (Figures 10 and 11). All values in both figures converge around 10^{22} cm^{-2} , the only difference is the visual extinction at which it is reached. In general, with high values of G_0 , hydrogen forms H_2 at higher visual extinctions. Figure 11 shows that for low values of n_H , H will form H_2 deeper into the cloud. At low visual extinctions ($A_v < 2$), curves that have low n_H/G_0 ratio are between 2 and 6 orders of magnitude lower than those with a high ratio.

6.5. Integrated Intensity

The integrated intensity (I) of the CO ($j = 1 \rightarrow 0$) line is shown in Figures 12 and 13. All values in both figures reach a value with a difference a factor of 2. The cooling rates in Figure 8 and 9 show different peak values and width of curves as density and radiation vary from this one might suspect that the black line in Figure 8 and the green line in Figure 9 are not as similar as they are in Figures 12 and 13. The effect of increasing the radiation consists of leading to lower values of I with respect to those for PDRs with lower G_0 . We also observe that a large G_0 PDR generates values of the integrated intensity of CO at larger visual extinctions than low G_0 PDRs. When the density is changed; high values for density lead to high values of integrated intensity at lower visual extinctions.

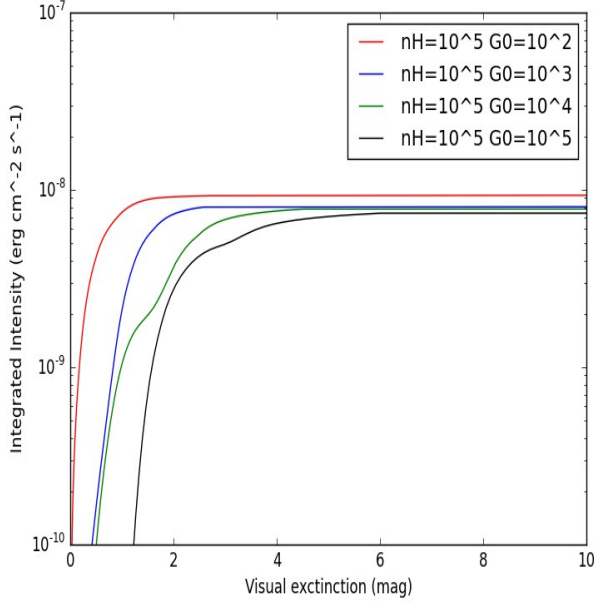


Figure 12: The integrated intensity of CO ($j = 1 \rightarrow 0$) transition for different types of PDR with constant density and varying G_0 .

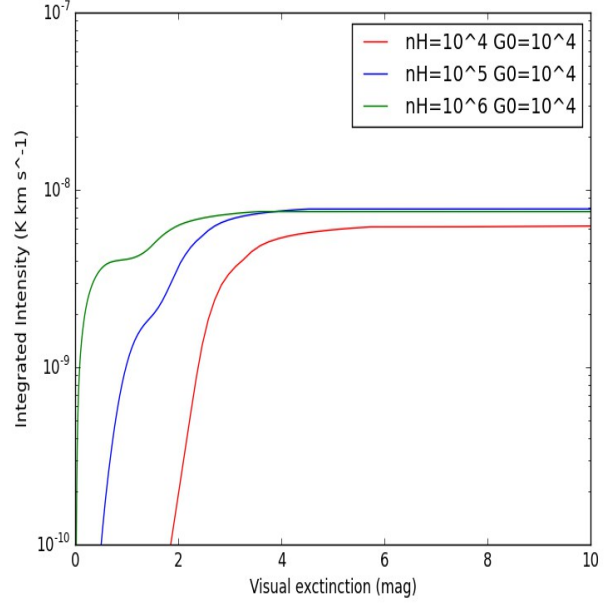


Figure 13: The integrated intensity of CO ($j = 1 \rightarrow 0$) transition for different types of PDR with constant G_0 and varying density.

6.6. The X_{co} factor

The X_{co} factor is shown in Figures 14 and 15. In these figures, we observe that for low visual extinctions $A_v < 2$ mag, the values of X_{co} are very high because of the low amount of CO in this visual extinction range due to the high radiation in the border of the cloud. Thereafter it reaches a minimum value, after which the value increases again due to the H_2 column density rising slowly. X_{co} increases around half an order of magnitude after $A_v > 2$ mag in both figures. All of the X_{co} values are within a factor 2 of each other at $A_v \geq 4$ mag. Increasing the radiation field leads to a higher minimum value, which is also located at larger visual extinctions than when we consider a low G_0 PDR (see Sect. 6.5). Increasing the density in Figure 15 leads to an opposite effect on the X_{co} factor as when we vary the values of G_0 because the emission of CO occurs within a thinner region due to the gas becoming optically thick at lower A_v .

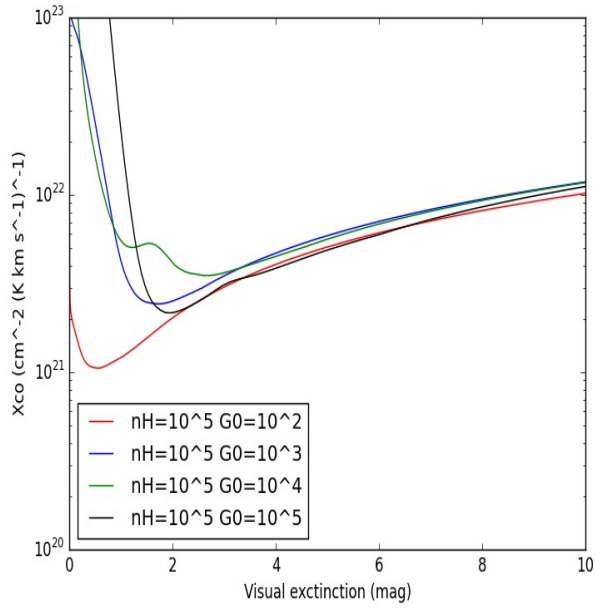


Figure 14: X_{CO} for different types of PDR with constant density and varying G_0 .

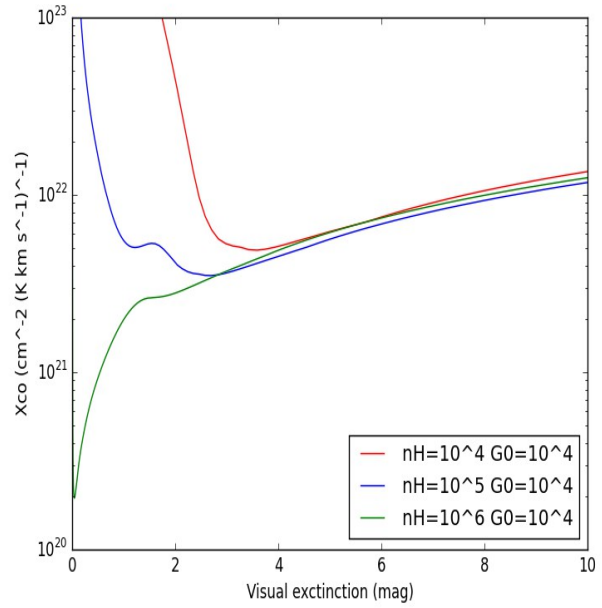


Figure 15: X_{CO} for different types of PDR with constant G_0 and varying density.

6.7. Surface chemistry effect

Figure 16 shows the effects of including surface chemistry on the X_{CO} factor. At $A_v < 6$ mag there is a minimal difference (factor 1.5 at most) between the curves. However, as the visual extinction increases, the differences between both curves becomes larger. In particular, deep into the cloud $A_v = 10$ mag, this difference is a factor of 2. This is because deeper into the cloud surface chemistry starts to have a larger effect on the formation of molecules like CO. This increase in CO abundance results in the difference between the curves shown in Figure 16.

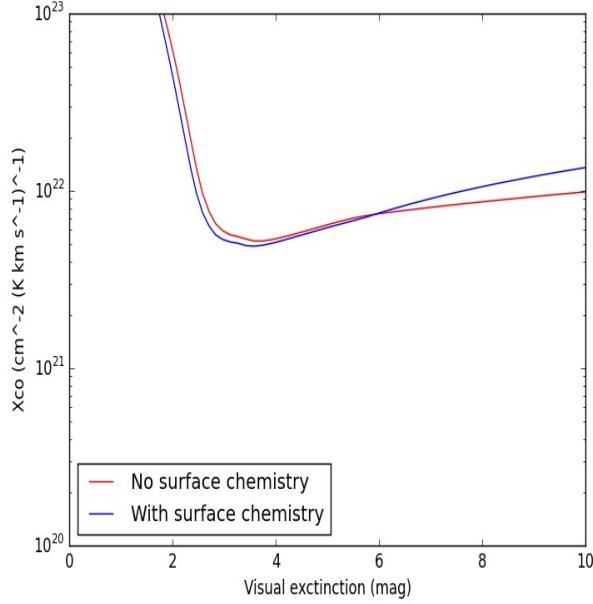


Figure 16: Comparison of the X_{co} curves with and without surface chemistry for $n_H=10^4 [cm^{-3}]$ and $G_0=10^4$

7. Comparison

7.1 Comparison with observations

We have compared the model results obtained for the X_{co} factor with observational results reported in Table 1. That table has observational values of X_{co} in the Milky Way. The observational values have been obtained using the methods described in Sect. 2. When comparing the values obtained in this work, it is evident that the values are 10-100 times larger than the observed X_{co} factor. Table 1 gives average values that are valid over large scales (Bolatto & Wolfire 2013), while the values obtained in this work are between $0 < A_v < 10$ mag. This difference is present in all the cases considered (different G_0 , n_H and inclusion or exclusion of surface chemistry). The H_2 column density matches what is observed, see Figure 3. This leads to the possibility that the difference might be due to the CO cooling rate. After an analysis, it was discovered that Expressions 3 and 7 both consider the cloud as being an semi infinite slab and the photons escaping form one direction. To remove this redundancy, we should omit the $1/2\pi$ in Expression (3). The result is a systematic error (factor $1/2\pi$) in the the integrated

intensity and X_{co} . With this correction, the X_{co} scales from $\sim 5 \cdot 10^{20}$ to $5 \cdot 10^{21} [\text{cm}^{-2} (\text{K km s}^{-1})^{-1}]$ in Figure 14 and from $2.3 \cdot 10^{19}$ to $5 \cdot 10^{21} [\text{cm}^{-2} (\text{K km s}^{-1})^{-1}]$ in Figure 15. These values are still systematically too high compared to observations. Nevertheless we should take into account that the observations in Table 1 are made in different parts of the Milky Way whereas this work only considers X_{co} in PDRs.

7.2 Comparison with previous works

The results that are obtained can also be compared to previous works to address the effect of the inclusion of surface chemistry. In this section, we compare our results to those from Bell et al. (2006). They used the UCL_PDR code (Papadopoulos et al. 2002; Bell et al. 2005). That code contains 128 species and over 1700 gas-phase reactions. The most important difference is that they neglect all dust grain chemistry, which is included in this work. In general, they consider lower values for the density and radiation strength ($10^2 \leq n_H \leq 10^4 [\text{cm}^{-3}]$ and $0.1 \leq G_0 \leq 10^5$).

In Figure 17, the cooling rate compared is lower and it has a different profile compared to Figures 8 and 9. This different cooling rate is the reason for the high X_{co} obtained in this work. This is even more visible when comparing Figure 18 to Figures 12 and 13; the integrated intensity is up to 10 times larger in Figure 18. Figure 18 also shows the H_2 column density which matches the results obtained in this work.

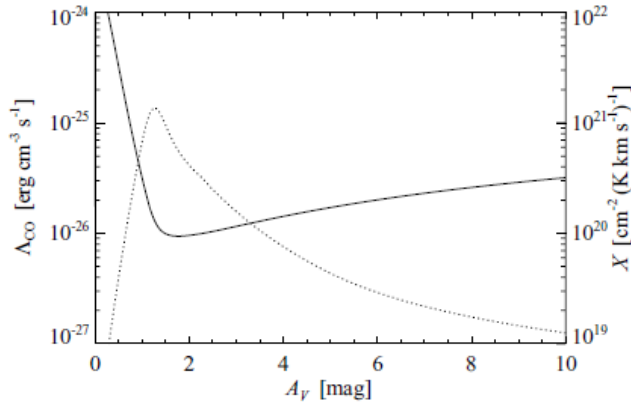


Figure 17: The dotted line is the CO cooling ($j = 1 \rightarrow 0$) rate. The solid line is X_{co} . For $G_0=1$ draine and $n_H=10^3 [\text{cm}^{-3}]$ Bell et al. 2006).

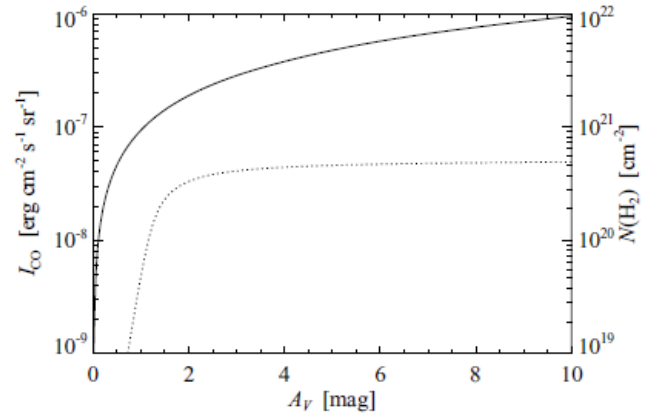


Figure 18: The dotted line is the integrated intensity. The solid line is the H_2 column density. For $G_0=1$ draine and $n_H=10^3 [\text{cm}^{-3}]$ Bell et al. 2006).

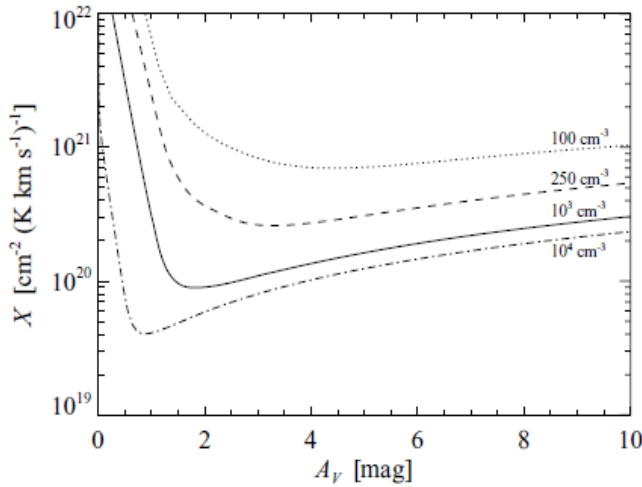


Figure 19: X_{co} for varying densities with $G_0 = 1$ draine (Bell et al. 2006).

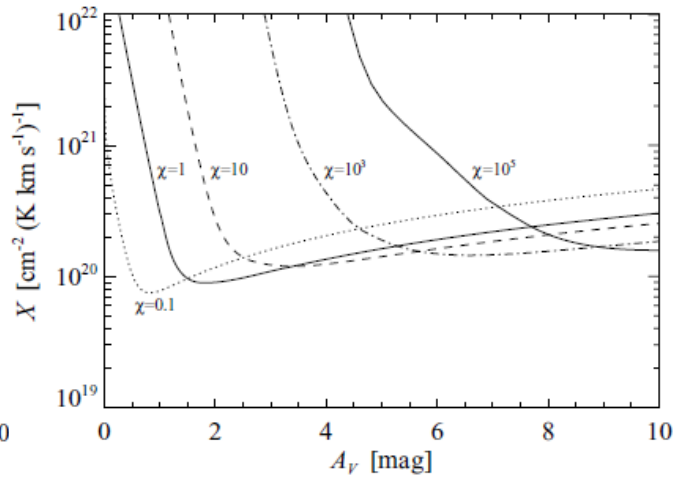


Figure 20: X_{co} for varying G_0 (X in the Figure) and constant density $n_{\text{H}}=10^3$ [cm^{-3}] (Bell et al. 2006).

The X_{co} in Figures 19 and 20 agree with the observational results in Table 1. This also means that X_{co} from this work is higher when compared to Figures 19 and 20. As mentioned earlier, this is due to the difference in cooling rates obtained with this work. In Figure 19 there is a very strong effect on X_{co} when increasing the density, which decreases X_{co} with a minimum value occurring at lower A_v . We find a similar behavior in our study, as shown in Figure. 15. The effects of density are less pronounced, especially at high visual extinction $A_v > 5$ mag compared to Bell et al. (2006), where lower densities are used. The effect of density could become less pronounced as the density increases. When comparing G_0 (Figure 20), the same general trends can be observed between (Bell et al. 2006) and this work. Both in figure 14 and 19 the minimum X_{co} occur deeper into the cloud as G_0 increases. The effect of surface chemistry can be seen and compared when looking at the slope of the curves in Figures 14, 15, 19 and 20 after the minimum peak has occurred. The slopes in this work are steeper due to the effects of surface chemistry (see Figure 16), while in Bell et al. (2006) the curves flatten out at high visual extinction $A_v > 5$ mag.

8. Conclusions

In this work, we have analyzed the X_{co} factor in photo-dissociation regions (PDRs) considering different types of PDRs by varying their physical and chemical parameters (density, intensity of the radiation field and presence of surface chemistry). The main conclusions obtained are:

- Including surface chemistry gives a lower (factor 1.5) X_{co} factor at low $A_v < 6$ mag and a higher value (factor 2) at high $A_v > 6$ mag.
- Increasing the density decreases the visual extinction where the CO is most abundant.
- Increasing the radiation field leads to a higher visual extinction range at which CO is most abundant.
- A higher radiation field gives a larger X_{co} factor.
- Increasing the density leads to a lower minimum value for X_{co} , which occurs closer to the surface of the cloud.
- The X_{co} factor obtained is 10 to a 100 larger than observations and previous works, likely due to the CO cooling rate and double inclusion of the fact that we consider an semi-infinite slab.
- It is useful to include surface chemistry as it does change X_{co} especially at high visual extinction $A_v > 6$ mag.

8.1 Future works

It is necessary to study the difference between these model results and the observation, by analyzing the cooling rate. It is necessary to shed light on the source these differences. One suggestion is to obtain the CO cooling directly from the model to avoid discrepancy. It will also be advisable to compare this work to observational results of PDRs with comparable densities and radiation.

9. References

- Bell T. A., Viti S., Williams D. A., Crawford I. A., Price R. J., 2005, *MNRAS*, 357, 961
- Bell, T. A., Roueff, E., Viti, S., Williams, D. A., 2006, *MNRAS*, 371, 1865
- Bolatto, A. D., Wolfire, M., Leroy, A. K., 2013, *ARA&A*, 51, 207-268
- Boulanger, F., Abergel, A., Bernard, J. P., Burton, W. B., Desert, F. X., et al. 1996, *A&A*, 312, 256–62
- Esplugues, G. B., Cazaux, S., Meijerink, R., Spaans, M., Caselli, P., et al. 2016, *A&A*, 591, A52
- Hollenbach, D. J., & Tielens, A. G. G. M., 1997, *ARA&A*, 35, 197-215
- Hollenbach, D. J., & Tielens, A. G. G. M., 1999, *Reviews of Modern Physics*, 71, 173-230
- Meijerink, R., & Spaans, M. 2005, *A&A*, 436, 397
- Murphy, E. J., Porter, T. A., Moskalenko, I. V., Helou, G., Strong, A. W., 2012, *ApJ*, 750, 126
- Papadopoulos P. P., Thi W.-F., Viti S., 2002, *ApJ*, 579, 270
- Pineda, J. L., Goldsmith, P. F., Chapman, N., Snell, R. L., Li, D., et al. 2010A, *ApJ* 721, 686–708
- Solomon, P. M., Rivolo, A. R., Barrett, J., Yahil, A., 1987, *ApJ*, 319, 730–41
- Tielens, A. G. G. M., & Hollenbach, D. J., 1984, *ApJ*, 291, 722
- Wakelam, V., Loison, J. C., Herbst, E., et al. 2015, *ApJS*, 217, 20
- Wilson, R. W., Jefferts, K. B., Penzias, A. A. 1970, *ApJ*, 161, L43
- Wilson, T. L., 1999, *Rep. Prog. Phy*, 62, 143–85
- Wolfire, M. G., Hollenbach, d., McKee, C. F., 2010, *ApJ* 716, 1191